A noise autocovariance model for SAR altimeter measurements with implications for optimal sampling

Ehlers, Frithjof; Slobbe, Cornelis; Verlaan, Martin; Kleinherenbrink, Marcel

DOI
10.1016/j.asr.2023.02.043

Publication date
2023

Document Version
Final published version

Published in
Advances in Space Research

Citation (APA)
Ehlers, F., Slobbe, C., Verlaan, M., & Kleinherenbrink, M. (2023). A noise autocovariance model for SAR altimeter measurements with implications for optimal sampling. *Advances in Space Research*, *71*(10), 3951-3967. https://doi.org/10.1016/j.asr.2023.02.043

Available online at www.sciencedirect.com

ScienceDirect

Advances in Space Research 71 (2023) 3951–3967

ADVANCES IN SPACE RESEARCH
(a COSPAR publication)

www.elsevier.com/locate/asr

A noise autocovariance model for SAR altimeter measurements with implications for optimal sampling

Frithjof Ehlers[a], Cornelis Slobbe[a], Martin Verlaan[b], Marcel Kleinherenbrink[a]

[a] Geoscience & Remote Sensing, Delft University of Technology (TU Delft), 2628 CN Delft, Netherlands
[b] Mathematical Physics, Delft University of Technology (TU Delft), 2628 CN Delft, Netherlands

Received 6 July 2022; received in revised form 27 February 2023; accepted 28 February 2023
Available online 6 March 2023

Abstract

Earlier work has empirically demonstrated some advantages of an increased posting rate of Synthetic Aperture Radar (SAR) altimeters beyond the expected ground resolution of about 320 m in Delay-Doppler (unfocused SAR, UFSAR) processing, corresponding to ~20 Hz sampling. Higher posting rates of 40–80 Hz were shown to prevent spectral aliasing of the signal, enable to measure swell wave related signal distortions and may lead to a reduced root mean square error of 1 Hz estimates of Sea Surface Heights (SSH), radar cross section (sigma0) and Significant Wave Heights (SWH) from current SAR altimeters. These improvements were explained by the narrow noise autocovariance function of the waveform signal's power speckle noise in along-track direction on one hand, and frequency doubling by power detection (squaring of the signal) on the other. It has not been explained, however, why the power speckle noise decorrelates faster than anticipated by the predicted Doppler resolution, and whether this decorrelation depends on the altimeter and processing configuration. Also, it has not been shown explicitly that the estimates of SSH, SWH and sigma0 decorrelate in the same way. Describing the noise autocovariance function – or equivalently the noise power spectral density via the Wiener-Kintchin theorem – is necessary on two counts: Knowing the noise autocovariance allows to apply optimal filtering strategies that maximize precision on one hand, while the noise power spectral density predicts the frequencies contained in the noise (and signals), which in turn determines the required sampling frequency according to the Nyquist theorem. Using a newly derived analytic noise autocovariance model for UFSAR-processed altimeter data, we show that the swift signal decorrelation is mainly due to the observation geometry. Furthermore, our results demonstrate that the noise autocovariance functions of power speckle, SSH, SWH and sigma0 estimates in along-track direction are different and depend on the sea state. On top of that, the noise autocovariance functions are strongly dependent on the number of Doppler beams used for multilooking, the used retracker, and the processing choices such as antenna gain pattern compensation and windowing within the UFSAR processing (Level-1b). We validated our noise autocovariance model with segments of 42 Sentinel-3B overpasses. Our findings are in accordance to all earlier work, but indicate that the reported precision improvements with respect to 20 Hz may have been too optimistic and that the SSH, SWH and sigma0 generally decorrelate slower than the power speckle noise. We found that the required posting rate is always higher or equal to 40 Hz. Our results will potentially enable improved spectral analysis and optimal filtering of any UFSAR altimetry data. More importantly, our results can be used to trade off different aspects for determining an optimal posting rate in UFSAR altimeter processing in different sea states and with changing processing parameters, which is necessary in view of strict precision requirements of existing and future SAR altimetry missions.

Keywords: Delay-doppler; 20 Hz; Posting rate; Sentinel-3; Sentinel-6 Michael Freilich; CryoSat-2

E-mail addresses: f.ehlers@tudelft.nl (F. Ehlers), d.c.slobbe@tudelft.nl (C. Slobbe), martin.verlaan@deltares.nl (M. Verlaan), m.kleinherenbrink@tudelft.nl (M. Kleinherenbrink)

https://doi.org/10.1016/j.asr.2023.02.043
0273-1177/© 2023 COSPAR. Published by Elsevier B.V.

1. Introduction

The advent of delay-Doppler altimeter data processing (Raney, 1998) and the launch of the first SAR altimeter CryoSat-2 started a new era of ocean remote sensing. In the meantime, data from the CryoSat-2, Sentinel-3, and Sentinel-6 Michael Freilich SAR altimeters have demonstrated the technique's capabilities to improve altimetric measurements of the worlds oceans by i) increasing the along-track resolution to about 320 m in comparison to conventional pulse-limited altimeters with about 7 km (Raney, 1998; Dinardo, 2020) and ii) increasing the precision of the geophysical estimates Sea Surface Height (SSH), Significant Wave Height (SWH), and radar cross-section (sigma0) (Wingham et al., 2006; Raney, 2012; Buchhaupt, 2019). One of the characteristics of delay-Doppler (in the following named unfocused SAR, UFSAR) processing is that waveforms can be focused (steered) to any ground location and at arbitrary posting rate (or, equivalently, ground distance). To avoid redundant information content in the data products, the overlap between consecutive waveforms in along-track direction is currently minimized by using a 20 Hz posting rate. This corresponds to about 320 m ground distance in UFSAR processing offered through the European Space Agency (ESA) (e.g. Dinardo, 2020; EUMETSAT, 2021, the exact value is dependent on the mission and orbit parameters). Talking about a 20 Hz sampling is hence not fully accurate, because it actually means the sampling according to an along-track ground spacing given by the resolution

$$L_x = \frac{cHf_p}{2Vf_cN_b}, \tag{1}$$

(see Eq. 14 in Ray et al., 2015) where c is the speed of light, H is the commanded tracker range (approximate range to the surface), f_p is the pulse repetition frequency, V is the satellite velocity tangential to the surface, f_c is the carrier frequency and N_b the number of pulses in a burst (used for coherent processing). Current SAR altimeter systems have been tuned in such a way that L_x corresponds to about 20 Hz in time domain, while the exact sampling frequency is varying over the course of an orbit.

Though L_x is the theoretical resolution of the UFSAR-processed altimeter data, some works report advantages of an increased posting rate of 40 Hz and 80 Hz, so a ground spacing of $L_x/2$ and $L_x/4$, respectively. Rieu et al. (2021b) demonstrated swell wave-related signal distortions in the waveform intensity and the estimates of Sea Level Anomaly (SLA), which are shown to be aliased in the case of 20 Hz sampling (Fig. 5 therein). Hence, in order to spectrally resolve these effects, the authors stress the need for a posting rate of at least 40 Hz and performed the analysis on 80 Hz. Buchhaupt (2019) suggests that the resolution L_x is applicable as long as the UFSAR waveform signal has not been absolute-squared, which is inherent to the UFSAR processing. Squaring doubles the bandwidth of a signal. Therefore, the waveform power, SSH, SWH, and sigma0 signals will contain frequencies of at least 20 Hz, requiring a 40 Hz sampling via the Nyquist theorem. This effect, explained in depth by Smith and Scharroo (2015) for the range direction, is why zero-padding of the waveform signal in range has become the default setting for Sentinel-6 Michael Freilich (EUMETSAT, 2021). The same logic applies to UFSAR-processed altimeter data in the along-track direction, which is in line with the aliasing reported by Rieu et al. (2021b).

Other works reported an increased precision of the estimated SWH, SSH, and sigma0 when using higher posting rates paired with subsequent averaging (Dinardo et al. (2015, 2021) and Buchhaupt (2019), chapter 5). Egido et al. (2021) calculated SWH, SSH and sigma0 at 80 Hz and subsequently averaged the estimates to 20 Hz. Following this strategy, the Root Mean Square Errors (RMSEs, with respect to a 1 Hz average) of SWH, SSH and sigma0 decreased by up to 34% for SWH, 30% for SSH and 25% for sigma0 in low sea state conditions (SWH of 1 m) and by 10–20% in higher sea state conditions (SWH of 4–7 m) when compared to the original 20 Hz data. The improvements were explained by the narrow noise autocorrelation function (noise ACF) of the waveform power signal in along track direction, which has a full width at half maximum of 100–150 m as opposed to $L_x \approx 320$ m. This swift decorrelation also caused the Effective Number of Looks (ENL) to increase from 20 to 40 to 80 Hz sampling. The ENL is a measure of the speckle noise reduction and resembles in theory the effective number of statistically independent samples that have been averaged (Quartly et al., 2001; Wingham et al., 2006; Egido and Smith, 2017; Scagliola et al., 2015a). Therefore, the higher the ENL, the higher the expected precision of the geophysical estimates. However, we will show later in this work that the behavior of the ENL at increased posting rates does not directly reflect the behavior of the estimates' precision.

In general, differences between a system's resolution and the correlation (statistical dependence) must be expected. For example, the pulse repetition frequency of conventional low resolution altimeters like (TOPEX, Jason 1–2–3) has been optimized to 2–4 kHz based on the expected pulse-to-pulse decorrelation and not on the effective footprint of several kilometers diameter. Another example is provided by LR-RMC (Low Resolution with Range Migration Correction) processing of SAR altimetry data (Phalippou and Demeestere, 2011; Moreau et al., 2021). This processing produces statistically independent 20 Hz estimates despite having an effective resolution of several kilometers. It is therefore important to describe the correlation (statistical dependence) instead of the resolution to leverage maximum precision. Up to this point it is unclear whether and how the findings from Egido et al. (2021) generalize to other missions and varying processing settings, and how the sea state dependence can be explained.

To fill this gap, we derive in this work a generic autocovariance model for the UFSAR-processed altimeter waveforms and the resulting SSH, SWH and sigma0 estimates.

The main assumption is that of a rough ocean surface, which is typically used also for the physical waveform models (e.g. Brown, 1977; Ray et al., 2015; Buchhaupt et al., 2018; Dinardo et al., 2021). The model is applicable to any SAR altimeter data as long as mission and instrument specific parameters are adjusted. This model can be used: i) to design optimal filters, ii) for advanced spectral analysis, and iii) to determine the optimal posting rate. Earlier studies have already outlined how to estimate the UFSAR precision based on assumptions on the speckle noise distribution (e.g. Phalippou and Enjolras, 2007). Hence, we put a higher emphasis on the along-track autocovariance functions (from which autocorrelation can be computed by normalization), than on the absolute precision.

The manuscript is organized as follows: We first outline the used data and the performed processing in Section 2. We describe the UFSAR processing, the retracking, and the used Sentinel-3B data. The section also provides a detailed description of how the autocovariance and autocorrelation functions of waveform image and retracked parameters are estimated from data. We also recap the known UFSAR Point Target Response (PTR) based on the expressions in Ray et al. (2015), which determines the theoretical resolution, because it will turn out in fact that the PTR and autocovariance function are closely related for the UFSAR-processed data. Our results (Section 3) are split into four parts. The first and third part present the measured speckle noise autocovariance functions and the measured noise autocovariance of the retracked parameters obtained from data, respectively. In the second and fourth part we accommodate the analytical derivations, aiming to reproduce our observations with our noise autocovariance model. Some limitations of our study are discussed in Section 4, our conclusions in Section 5.

2. Methods and data

2.1. Terminology

The altimeter's UFSAR return signal is called a waveform, and is most often visualized as power over range. However, once consecutive UFSAR-processed waveforms are properly referenced to the same height, it is often more practical to imagine them as an image $P(r,x)$ with coordinates range r and along-track distance x (see Fig. 2A). Indeed, SAR altimetry waveforms are essentially nothing else than a SAR image from a nadir-looking angle. We will use this notion extensively in the remainder and refer to the UFSAR-processed waveforms as $P(r,x)$ or waveform image. To ease readability of the manuscript, a list of mathematical symbols and their meaning is provided in Table 1.

2.2. Sentinel-3 data

For our analysis we use SRAL Level-1a data from Sentinel-3B over the North Sea, relative orbit number 370, spanning the three year period between December 2018 to December 2021. To mitigate the effects of changing orbit parameters (implying changing resolution L_x) on one hand and to limit the variability in the retracked sigma0 and SWH along-track on the other, we process the data between the latitudes 52.4 and 53 degrees North, which corresponds to a 70 km long segment of the sea surface. In total, there are 42 overpasses. The L1a processing baselines are 003 and 004. The Level-1a data were obtained from EUMETSAT's dissemination services via https://eo-portal.eumetsat.int.

2.3. UFSAR (unfocused SAR, delay-Doppler) processing

Similar to the works of Egido and Smith (2017); Egido et al. (2021); Ehlers et al. (2022), we use a modified Fully-Focused SAR (FFSAR) processor to obtain UFSAR waveforms of Sentinel-3B at high posting rates (waveforms are provided at 0.5 m distance on ground). A high posting rate is needed for the evaluation of the ACF at small along-track distances. For an overview of UFSAR processing we refer the reader to Dinardo (2020). Our FFSAR processor is a continued development of the CryoSat-2 implementation in Kleinherenbrink et al. (2020) and is introduced in Ehlers et al. (2022). The emulated UFSAR processing is explained in more detail in Ehlers et al. (2022, Section 2.3 and Appendix B). For a validation of our emulated UFSAR processing, we refer the reader to the Appendix B in (Ehlers et al., 2022). It must be stressed that the FFSAR phase calibrations outlined in Ehlers et al. (2022, Appendix A, Tracker range phase jumps) have no effect on the UFSAR waveforms, because in the UFSAR case coherent integration is only performed over individual bursts. The resulting multilooked UFSAR waveforms are by default referenced to the same height over the reference ellipsoid WGS84. If not stated otherwise explicitly, we will use 180 bursts along the aperture for UFSAR multilooking. That is, 180 Doppler beams in the Doppler beam stack, corresponding to ~ 2.3 s along the satellite aperture.

2.4. Level-2 processing (retracking)

As in Ehlers et al. (2022), the SSH and SWH are obtained from the UFSAR waveforms by a retracking based on the SAMOSA2 physical waveform model (Ray et al., 2015; Dinardo, 2020). For our purposes, retracking the data on about 240 Hz suffices. This corresponds to a twelve times denser sampling than the default (20 Hz), meaning about 27 m ground spacing.

2.5. Theoretical resolution – UFSAR point target response

The theoretical resolution of UFSAR-processed data is determined by the instrument's PTR, which describes the observed return echo from a single point scatterer close to the surface. According to Ray et al. (2015, Eq. 22) the power of the PTR for the l-th Doppler beam and in the k-th range gate is approximated by

Table 1
List of symbols used in the text.

Symbol	Description
H	altimeters' tracker range
f_p	altimeters' pulse repetition frequency
V	altimeters' velocity tangential to the surface (not ground projected)
c	speed of light in vacuum
f_c	altimeters' carrier frequency
N_b	number of pulses per altimeter burst
s	altimeters' chirp slope
B	altimeters' chirp bandwidth
G_x	altimeters' antenna gain pattern
L_x	theoretical along-track resolution after UFSAR processing
L_r	altimeters range resolution
h^2	UFSAR point target response in units of power
h_m^2	multilooked UFSAR point target response in units of power
k	range gate index within the waveform image
m	along-track index within the waveform image
l	Doppler beam index
b	burst index
t_b	timing of burst b relative to the satellites nadir position
T_m	the time along the satellites' aperture corresponding to all bursts (Doppler beams) used for multilooking
x	along-track distance in waveform image $x = m\Delta x$
r	range distance in waveform image $r = k\Delta r$
Δx	along track distance corresponding to posting rate
Δr	range distance between two range gates in waveform image
y	cross-track distance perpendicular to altimeter ground track
z	elevation from altimeter ground track
$\mathcal{C}$	used as placeholder for any non-essential pre-factor throughout the manuscript
$\boldsymbol{r}$	shorthand notation for the 2D coordinate vector $(r\,x)^\intercal$
$P(\boldsymbol{r}) = P_{k,m}$	power values of the multilooked UFSAR waveform image in continuous and discrete notation
$C_f(\boldsymbol{r}) = C_{f\;k,m}$	2D-autocovariance function of variable f in continuous or discrete formulation
$C_f(x) = C_{f\;m}$	1D-autocovariance function in along-track direction of variable f in continuous or discrete formulation
$R_f(\boldsymbol{r}) = R_{f\;k,m}$	2D-autocorrelation function of variable f in continuous or discrete formulation
$R_f(x) = R_{f\;m}$	1D-autocorrelation function in along-track direction of variable f in continuous or discrete formulation
$\rho(\boldsymbol{r}) = \rho_{k,m}$	power speckle noise values of the multilooked UFSAR waveform image in continuous and discrete notation
$\mathbb{E}[\ldots]$	denoting the ensemble mean of the property within brackets
$P_b(\boldsymbol{r})$	power values of the singlelooked UFSAR waveform image using only burst b at time lag t_b
$\rho(\boldsymbol{r})_b = \rho_{b\;k,m}$	power speckle noise values of the singlelooked UFSAR waveform image using only burst b at time lag t_b
ε	fictive true, complex-valued waveform image (amplitudes and phases)
η and μ	real and imaginary part of ε
σ^2	variance of the normally distributed η and μ with unit of power
$\delta_{k,k'}$	Kronecker-delta evaluated at indices k and k'
$\boldsymbol{P}$	single column vector P_k of the UFSAR waveform image $P_{k,m}$
$\boldsymbol{\rho}$	single column vector ρ_k of the UFSAR speckle noise image $\rho_{k,m}$
$\boldsymbol{\beta}$	parameter vector containing the parameters estimated during retracking (epoch, SWH, Pu)
$\boldsymbol{\epsilon}_\beta$	noise of the estimated $\boldsymbol{\beta}$
$\boldsymbol{P}^{\text{model}}(\boldsymbol{\beta})$	physical waveform model of the UFSAR-processed ocean return echo (here we use SAMOSA2)
$\mathbf{J}$	Jacobian matrix of the used retracker (waveform model) $J_{kj} = \partial P_k^{\text{model}}(\boldsymbol{\beta}^*)/\partial\beta_j$
$\mathbf{W}$	weighting matrix that propagates speckle noise $\boldsymbol{\rho}$ into noise of parameter estimates $\boldsymbol{\beta}$
$\boldsymbol{W}_{\text{estimate}}$ or $\boldsymbol{W} = W_k$	weighting vector (single row of $\mathbf{W}$) for obtaining the noise of the specific parameter with name "estimate"

$$h^2(k,l) \approx \mathcal{C}\mathrm{sinc}^2\left[\frac{x}{L_x} - l\right]\mathrm{sinc}^2[k - k_l], \tag{2}$$

with along-track ground distance x, along-track resolution L_x, range offset k_l and range gate number k proportional to the range r relative to the tracker range within the range window. Detailed variable definitions are provided in the given reference and are omitted here for brevity. The first sinc^2-term determines the along-track resolution L_x for each individual Doppler beam. However, the multilooked waveforms are formed from the sum of multiple Doppler beams within the aperture that point from bursts with index $b \in \mathbb{N}$ towards the same ground position, see Fig. 1A. Similarly, all Doppler-beam waveforms are added up within the SAMOSA waveform models (Ray et al., 2015; Dinardo, 2020). The Doppler beams point to the target with different looking angles and are thus weighted with the instrument's azimuth antenna gain power pattern $G_x^2(x)$ (Ray et al., 2015; Scagliola et al., 2015a). So in order to describe the multilooked PTR power h_m^2, one needs to perform a weighted summation of Eq. 2 over all beams towards the same target. For a target at along-track dis-

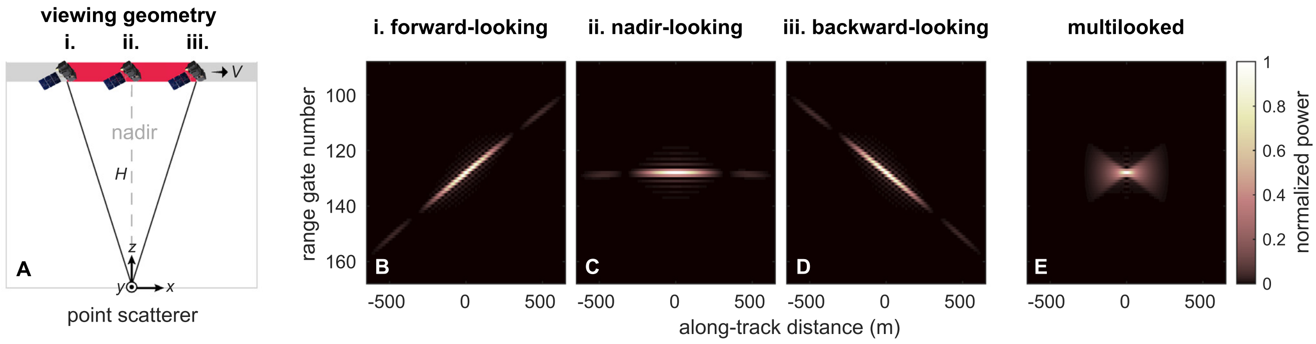

Fig. 1. Panel A: Viewing geometry of the satellite with positions i., ii. and iii.; The panels B–E show the (multiloooked) point target responses (PTR) according to Eq. 2 or equivalently Eq. 3. Panel B and D: When using the Doppler beams from a single forward-looking or backward-looking burst (i. and iii.) to produce waveforms in the vicinity of a point target (Dinardo, 2020, equivalent to 'Beam steering'), the target appears tilted in the waveform data; Panel C: When using the Doppler beams from a single nadir-looking burst (ii.) to produce waveforms in the vicinity of a point target, the target appears straight in the waveform data; Panel E: In the multilooked waveforms all these patterns are overlapping, hence forming a bow tie pattern (see also Ehlers et al., 2022).

tance $x = 0$, cross-track distance y, and height z, centered on the Earth's surface, h_m^2 can be shown to be (see Appendix B)

$$h_{\mathrm{m}}^2(r,x) \approx \mathcal{C}\mathrm{sinc}^2\left[\frac{x}{L_x}\right]\sum_{t_b} G_x^2(Vt_b)\ \mathrm{sinc}^2\left[\frac{2B}{c}(r-r_b)\right] \tag{3}$$

with

$$r_b = \frac{xV}{H}t_b + \frac{x^2}{2H} + \frac{y^2}{2H} - z - \frac{xf_cV}{Hs} \tag{4}$$

in the approximation of a flat Earth, constant satellite tangential velocity V and parabolic range history over the synthetic aperture. Here, c is the speed of light in vacuum, B the chirp bandwidth, $t_b \in [-T_{\mathrm{m}}/2, T_{\mathrm{m}}/2]$ the relative burst timings with respect to nadir, T_m the multilooking time, s the chirp slope, $T_b = N_b/f_p$ the burst duration and N_b number of pulses in a burst. We will use the term multilooking time T_m for the time corresponding to the actually available or used number of bursts. The individual terms of h_m^2 – i.e., Eq. 3 evaluated for a single, fixed t_b – are illustrated in Fig. 1 B-D. It can be seen that the PTR at off-nadir angles is generally tilted with respect to the (r,x)-coordinates. This tilt is caused by the linear leading term in the range offset $r_b(x) = Vt_b/Hx + \mathcal{O}(x^2)$. Once the Doppler beams from all looking angles between satellite positions i. and iii. are multilooked (added), the multilooked PTR significantly deviates from its single contributors, see Fig. 1E, and forms a bow tie pattern as observed in Ehlers et al. (2022). As the PTR is the transfer function of the altimeter, we expect similar patterns to arise in the waveforms' speckle noise as well.

2.6. Two-dimensional speckle noise autocorrelation function

In this section we evaluate and analytically approximate the noise autocorrelation function (ACF) of the multilooked waveforms $P(r,x)$. We shorthand denote the coordinates (r,x) as vector $\boldsymbol{r}$.

2.6.1. Definition

The autocovariance function of a variable f is defined as

$$C_f(\boldsymbol{r}_1,\boldsymbol{r}_2) = \mathbb{E}[(f(\boldsymbol{r}_1) - \mathbb{E}[f(\boldsymbol{r}_1)])^*(f(\boldsymbol{r}_2) - \mathbb{E}[f(\boldsymbol{r}_2)])], \tag{5}$$

where $\mathbb{E}[\cdot]$ denotes the expectation (ensemble average) and $\cdot^*$ the complex conjugate, which can be omitted for real-valued functions such as power. The autocorrelation is the normalized autocovariance such that $R_f(\boldsymbol{r},\boldsymbol{r}) = 1$ for all $\boldsymbol{r}$, namely

$$R_f(\boldsymbol{r}_1,\boldsymbol{r}_2) = \frac{C_f(\boldsymbol{r}_1,\boldsymbol{r}_2)}{\sqrt{\mathbb{E}\left[|f(\boldsymbol{r}_1) - \mathbb{E}[f(\boldsymbol{r}_1)]|^2\right]\mathbb{E}\left[|f(\boldsymbol{r}_2) - \mathbb{E}[f(\boldsymbol{r}_2)]|^2\right]}}. \tag{6}$$

Speckle noise $\rho(\boldsymbol{r})$ is defined here as the deviation of $P(\boldsymbol{r})$ from its expected value

$$\rho(\boldsymbol{r}) = P(\boldsymbol{r}) - \mathbb{E}[P(\boldsymbol{r})]. \tag{7}$$

In general, the mean power and hence the standard deviation of the speckle noise ρ changes within the waveform with range and with changing SSH, SWH and sigma0 in along-track direction, making the image statistics instationary. For now, we want to assume stationarity, which we will discuss later on. With this assumption, the autocorrelation function is only dependent on the distance vector between two locations in the image, and hence

$$C_\rho(\boldsymbol{r}) = \mathbb{E}[\rho(0)\rho(\boldsymbol{r})], \tag{8}$$

$$R_\rho(\boldsymbol{r}) = \frac{\mathbb{E}[\rho(0)\rho(\boldsymbol{r})]}{\sqrt{\mathbb{E}\left[\rho(0)^2\right]\mathbb{E}\left[\rho(r)^2\right]}} = \frac{\mathbb{E}[\rho(0)\rho(\boldsymbol{r})]}{\mathbb{E}\left[\rho(0)^2\right]} \tag{9}$$

holds.

2.6.2. Estimation of two-dimensional speckle noise autocorrelation function from data

As outlined above, the obtained waveforms are not just noise and the mean power and noise standard deviation are continuously varying over the waveform image (see e.g.

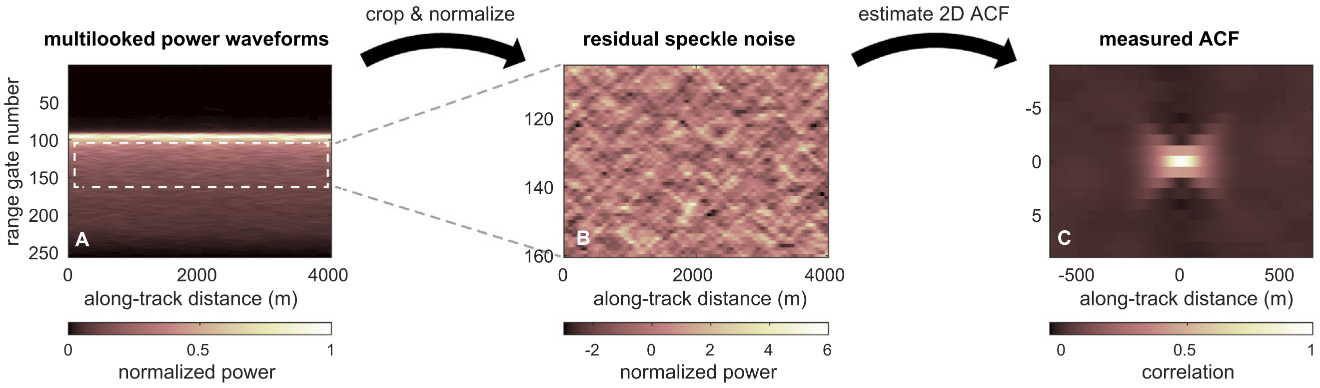

Fig. 2. Workflow for calculation of the 2D speckle noise ACF for one Sentinel-3B overpass, according to Section 2.6.2.

Fig. 2A). Hence, we are faced with the problem of separating signal and noise, without knowing the ensemble mean $\mathbb{E}[P]$. To do so, we normalize the waveforms in a way that they approximately obey to stationary statistics, so that the spatial average can be used instead of the ensemble mean to calculate the speckle noise ACF. Our workflow is summarized in Fig. 2A–C and explained in the following.

In this analysis, the leading edge of the waveform data is excluded since small range misalignments between consecutive waveforms are inevitable and have highest effect where the gradient in range is highest. Furthermore, the waveform tail is excluded, since it is not seen by all Doppler beams (e.g. EUMETSAT, 2021, see Section 7.3.13.4.1 Geometry mask), which would affect the statistics. We first crop the discrete waveform image $P_{k,m}$ with range index $k = 1, \ldots, 256$ and along-track index $m = 1, \ldots, M$ to range gates $105 \leqslant k \leq 160$ (with zero-padding), which is about 15 range gates behind the leading edge. We then normalize variations in along-track direction by first dividing with the column-wise mean

$$\widehat{P}_{k,m} = \frac{P_{k,m}}{\frac{1}{56}\sum_{k'} P_{k',m}} \tag{10}$$

and consecutively divide by the row-wise mean

$$\hat{\widehat{P}}_{k,m} = \frac{\widehat{P}_{k,m}}{\frac{1}{M}\sum_{m'} \widehat{P}_{k,m'}} \tag{11}$$

to compensate the fading of the waveform tail. Since the speckle noise of a multilooked waveform is in good approximation chi-square distributed (Quartly et al., 2001), mean and noise standard deviation are proportional to each other. Therefore, normalizing $\hat{\widehat{P}}_{k,m}$ to unit mean makes also the noise standard deviation of the speckle noise constant. Finally, we define the residual speckle noise ρ as

$$\rho_{k,m} = \frac{\hat{\widehat{P}}_{k,m} - \mathrm{mean}\left(\hat{\widehat{P}}_{k,m}\right)}{\mathrm{std}\left(\hat{\widehat{P}}_{k,m}\right)}, \tag{12}$$

which should then be approximately statistically stationary with zero mean and unit standard deviation, see Fig. 2B for an illustration. The speckle noise autocorrelation function $R_{\rho\ k,m}$ can then be evaluated via Eq. 9 and is shown in Fig. 2C. In this example we recover an ACF that qualitatively resembles the bow tie pattern of the multilooked PTR when compared to Fig. 1E. In Section 3 we will analytically derive the relation between the speckle noise ACF $R_\rho(\boldsymbol{r})$ and the multilooked PTR h_m.

2.7. Estimating the along-track noise autocorrelation of the retracked parameters and geophysical estimates

For calculating the noise ACF $R_{\mathrm{parameter}}(x)$ of the retracked parameters, we use the same definition as before (Eq. 9). Since the retracked parameters are generally not constant over the track segment, we first detrend them by removing a 1 Hz moving median (similar to Egido et al., 2021). Furthermore, we consider values beyond four times the median absolute deviation as outliers and set them to NaN. Pairs with NaNs are simply omitted in the estimation of the noise ACFs. In a total of six overpasses, the outlined detrending did not produces satisfactory results for at least one of the considered variables. Therefore, these six overpasses have been omitted in the analysis, leaving a remaining number of 36 Sentinel-3B overpasses in total.

3. Results

3.1. Measured 2D speckle noise autocorrelation functions

Fig. 3 shows the residual speckle noise images (second column) for varying multilooking scenarios (first column, varying amount of Doppler beams used for multilooking). The corresponding measured 2D speckle noise ACF is provided in the third column. In general, the residual speckle noise images may remind of ocean wave patterns but are in this case not related to ocean waves at all, as will be shown later. As mentioned earlier, the speckle noise ACF in the first row A resembles qualitatively the bow-tie pattern of the multilooked PTR in Fig. 1E. Furthermore,

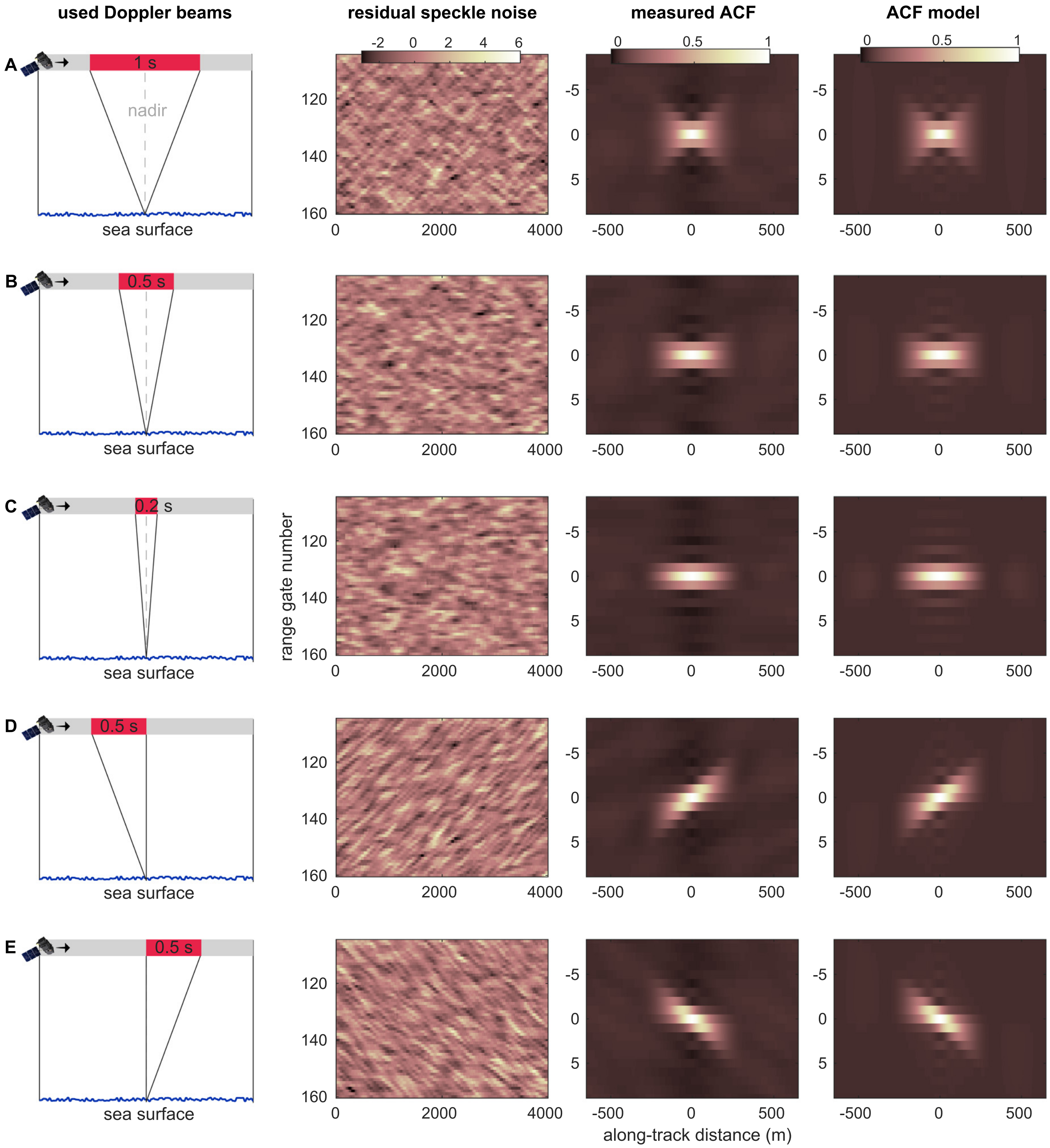

Fig. 3. Analysis of residual speckle noise images (according to Section 2.6.2 and Fig. 2) for different multilooking times T_m and one Sentinel-3B overpass. Rows A–C show the influence of reducing the multilooking time from 1 s to 0.5 s to 0.2 s (number of multilooked Doppler beams: 78, 39 and 16). Rows D and E show the effect of using the forward-looking and backward-looking fraction of bursts along the aperture only. The corresponding measured 2D speckle noise ACFs are shown in the third column, the ACF model according to Eq. 27 in the fourth column. The patterns in the residual speckle noise are in this case fully explained by the model (different observation geometry) and may not be mistaken for the imprint of ocean waves.

when using either only forward-looking or backward-looking Doppler beams (rows D and E), we observe a similar tilt as illustrated in Fig. 1B,D. We can conclude that the 2D speckle noise ACF in Fig. 3 is strongly dependent on the number of Doppler beams that is used for multilooking and their viewing geometry. Particularly interesting to notice is that the speckle noise ACF along the range gate 0 is narrower, the more Doppler beams are used for multilooking, see rows A-C. Hence, the decorrelation of the speckle noise along individual range gates (as presented in Egido et al., 2021) changes.

3.2. Analytical derivation of the two-dimensional speckle noise autocorrelation

In the following we attempt to simplify Eq. 8 with the goal to explicitly write it in terms of the altimeters' parameters and UFSAR-processing configuration. First we express the waveform image $P(\mathbf{r})$ as a summation over multiple Doppler beams with index b (for burst), hence $P(\mathbf{r})$ can be rewritten as $\sum_b P_b(\mathbf{r})$. Inserting this into Eq. 7 and using linearity of the sum and the expectation operators yields

$$\rho(\mathbf{r}) = \sum_b P_b(\mathbf{r}) - \mathbb{E}[P_b(\mathbf{r})] = \sum_b \rho_b(\mathbf{r}) \tag{13}$$

where ρ_b means the speckle noise in each single Doppler beam waveform before multilooking. Plugging this result into Eq. 8 yields diagonal and cross terms of the form $\mathbb{E}[\rho_b\rho_b]$ and $\mathbb{E}[\rho_b\rho_{b'}]$ with $b \neq b'$, respectively. Due to the decorrelation of the ocean surface and the strongly varying phases of the scattering facets from burst to burst, the speckle noise ρ from Doppler beams of different bursts is here assumed uncorrelated, and hence the cross terms vanish, i.e. $\mathbb{E}[\rho_b\rho_{b'}] = \mathbb{E}[\rho_b]\mathbb{E}[\rho_{b'}] = 0$. Therefore we can simplify Eq. 8 to

$$\mathbb{E}[\rho(0)\rho(\mathbf{r})] = \mathbb{E}\left[\sum_b \rho_b(0) \sum_{b'} \rho_{b'}(\mathbf{r})\right] \tag{14}$$

$$= \sum_b \mathbb{E}[\rho_b(0)\rho_b(\mathbf{r})]. \tag{15}$$

This is our first meaningful result: The speckle noise autocovariance function of the multilooked waveforms is provided by the sum of speckle noise autocovariance functions of Doppler beams from individual bursts, presuming independence. Expressed in terms of P_b those summands are written

$$\mathbb{E}[\rho_b(0)\rho_b(\mathbf{r})] = \mathbb{E}[P_b(0)P_b(\mathbf{r})] - \mathbb{E}[P_b(0)]\mathbb{E}[P_b(\mathbf{r})]. \tag{16}$$

In order to proceed, we now need to find an explicit expression of $P_b(\mathbf{r})$. Imagine that $\varepsilon_b(\mathbf{r})$ was the true, complex-valued waveform image (amplitudes and phases, before taking the absolute square) of burst b *in absence of resolution constraints*. Since the altimeter is a linear system and has limited resolution, expressed by its PTR or transfer function $h_b(\mathbf{r})$, see Eq. B.2, the complex-valued receive signal is given by the convolution of PTR and the hypothetical, true waveform image (e.g. Engen and Johnsen, 1995). As the waveform images are absolute-squared before multilooking, the absolute square of this convolution resembles P_b, namely

$$P_b(\mathbf{r}) = |(\varepsilon_b * h_b)(\mathbf{r})|^2, \tag{17}$$

where $(f * g)(\mathbf{r})$ means the convolution of f and g evaluated at $\mathbf{r}$. Now, Eq. 17 can be inserted into the expression for the speckle noise ACF in Eq. 16, which is then determined by the statistics of the true return signal $\varepsilon_b(\mathbf{r})$ and the shape of the PTR $h_b(\mathbf{r})$.

The complex valued waveform image ε can be modeled as the coherent sum of many (N) different scatterers

$$\varepsilon = V\exp(j\varphi) = \sum_{n=1}^{N} V_n \exp(j\varphi_n), \tag{18}$$

where V_n and φ_n are amplitude and phase of the n-th scatterer (Goodman, 1976; Jakeman and Pusey, 1976). If the surface roughness is high compared to the Radar's wavelength and if $N \gg 1$, then ε can be regarded as the result of a two-dimensional random walk in the complex plane and therefore both its real part $\mathrm{Re}(\varepsilon) = \eta$ and imaginary part $\mathrm{Im}(\varepsilon) = \mu$ follow independent Gaussian distributions with zero mean and same variance and $\varepsilon = \eta + j\mu$ (Goodman, 1976; Jakeman and Pusey, 1976). In this case, its absolute squared $|\varepsilon|^2$ is exponentially distributed, which has been successfully exploited in the altimetry field already (e.g. Quartly et al., 2001; Gómez-Enri et al., 2007; Buchhaupt, 2019). This is also called the case of fully-developed speckle and is assumed throughout this work. Additionally, we want to assume that ε is spatially white with constant variance σ^2. In summary, the statistics of the image $\varepsilon_{k,m}$ are constrained to

$$\eta, \mu \sim \mathcal{N}\left(0, \sigma^2\right) \tag{19}$$

$$\mathbb{E}\left[\eta_{k,m}\eta_{k',m'}\right] = \sigma^2\delta_{k,k'}\delta_{m,m'} = \mathbb{E}\left[\mu_{k,m}\mu_{k',m'}\right]. \tag{20}$$

Finally, using the Assumptions 19, 20 allows to explicitly write Eq. 16 through Eq. 17, as outlined in Appendix A. Under the condition that the PTR $h_b(\mathbf{r})$ was separable into $h_b(\mathbf{r}) = R_b(r)X_b(x)$, the speckle noise autocovariance Eq. 16 becomes

$$\mathbb{E}[\rho_b(0)\rho_b(\mathbf{r})] = 4\sigma_b^4|(h_b * h_b)(\mathbf{r})|^2. \tag{21}$$

However, the condition of separability is not met with $h_b(\mathbf{r})$ as in Eq. B.2. We will explain in the following two paragraphs that this shortcoming can be fixed via a variable transform.

The simplified case: Let us first discuss the simple but related case, where this holds true, namely $h'_b(\mathbf{r}) = \mathcal{C}\mathrm{sinc}^2(x/L_x)\mathrm{sinc}^2(r/L_r)$ with $L_r = 2B/c$. This case is special in the sense that the convolution of a sinc-function with itself yields again the same sinc-function (though scaled in amplitude), as can be derived by using the Fourier convolution theorem and knowing that the transform pair of a sinc is a boxcar-function. This would yield

$$\mathbb{E}\left[\rho'_b(0)\rho'_b(\mathbf{r})\right] = \mathcal{C}\sigma_b^4\mathrm{sinc}^2\left(\frac{x}{L_x}\right)\mathrm{sinc}^2\left(\frac{r}{L_r}\right), \tag{22}$$

which is again the PTR up to a numerical factor $\mathcal{C}$ and the pre-factor σ_b^4 that has units of power squared.

The case at hand: With the simple case in mind, we can continue with the actual PTR $h_b(r,x) = \mathrm{sinc}((r - r_b(x))/L_r)\mathrm{sinc}(x/L_x)$, which contains a range offset $r_b(x)$ depending on x. However, with the variable transform

$$x' = x \tag{23}$$

$$r' = r - r_b(x) \tag{24}$$

we recover the above-discussed simpler case $h'_b(r', x') = \mathrm{sinc}(r'/L_r)\mathrm{sinc}(x'/L_x)$. Since the determinant of the Jacobian of the given variable transform is strictly equal to 1 and the transform does not flip the sign of integration, all the considered convolutions that lead to Eq. 22 remain unchanged as well. Hence, we can obtain the speckle noise ACF of each Doppler beam by simply reversing the variable transform in Eq. 22 again in the end, and hence obtain

$$\mathbb{E}[\rho_b(0)\rho_b(\boldsymbol{r})] = \mathcal{C}\sigma_b^4\mathrm{sinc}^2\left(\frac{x}{L_x}\right)\mathrm{sinc}^2\left(\frac{r-r_b(x)}{L_r}\right). \tag{25}$$

Using that the power σ_b^2 of a single Doppler beam contribution is proportional to the antenna gain power pattern $G_x^2(Vt_b)$ and plugging the result into Eq. 15, we can then write the speckle noise ACF of the multilooked waveform image as

$$\begin{aligned} C_\rho(\boldsymbol{r}) &= \mathbb{E}[\rho(0)\rho(\boldsymbol{r})] \\ &= \mathcal{C}\mathrm{sinc}^2\left[\frac{x}{L_x}\right]\sum_b G_x^4(Vt_b)\mathrm{sinc}^2\left[\frac{2B}{c}(r-r_b(x))\right] \end{aligned} \tag{26}$$

and its autocorrelation function as

$$R_\rho(\boldsymbol{r}) = N_R\mathrm{sinc}^2\left[\frac{x}{L_x}\right]\sum_b G_x^4(Vt_b)\mathrm{sinc}^2\left[\frac{2B}{c}(r-r_b(x))\right] \tag{27}$$

with normalization factor $N_R = 1/\sum_b G_x^4(Vt_b)$. Besides the different weighting, this expression is almost identical to the multilooked PTR from Eq. 3. Therefore, the resemblance of the multilooked PTR from Fig. 1E and the ACF from Fig. 2C is no coincidence. It must be stressed though that there would be lesser correspondence in case of windowing, which alters the PTR shape. The reason is that $(h_b * h_b)(\boldsymbol{r}) = \mathcal{C}h_b(\boldsymbol{r})$ (compare Eq. 21) does not generally hold true, which would cause that the summands of the speckle noise ACF and PTR showed different functional dependence.

The modeled speckle noise ACF $R_\rho(\boldsymbol{r})$ is plotted in the rightmost column of Fig. 3 for the different multilooking scenarios. The model shows absolute differences with the measured ACF no higher than 0.05 and captures the complex dependence on the illumination geometry. In this comparison, we observe that the values of the measured noise ACF are slightly lower around $x = 0$, typically around -0.02. We suspect that this is an artifact of the empirical normalization step (see Section 2.6.2). Alternatively, it might be caused by bursts leaving and entering the aperture as the UFSAR processing progresses in along-track direction: We start with Doppler beams from bursts 1 to 180, but once we have progressed by a distance corresponding to one burst repetition interval (about 80 m on ground for Sentinel-3B), we consider bursts 2 to 181 instead. This aspect is not captured by the model, but present in the data.

By inspection of Fig. 3A–C one notices that the ACF $R_\rho(r = 0, x)$ becomes narrower in along-track direction, the more Doppler beams are being used for multilooking. This means, when considering a single range gate only, we find a much quicker decorrelation than anticipated by the sinc^2-function and the theoretical resolution L_x, as reported before by Egido et al. (2021). This behavior is illustrated in Fig. 4A, which shows the modeled $R_\rho(r = 0, x)$ alongside $\mathrm{sinc}^2(x/L_x)$ and Sentinel-3 data using 180 bursts for multilooking. Model and data agree to about 0.02, while the sinc^2-function is off by up to 0.5. In general this decorrelation behavior is dependent on the processing settings such as the used number of Doppler beams, antenna gain pattern compensation and windowing, and the mean square slope of the sea surface (considered as high for a rough surface). Furthermore, due to the nontrivial two-dimensional shape of the speckle noise ACF, this swift decorrelation is not representative for every variable obtained from the waveform image. One of many counter examples is the cumulated power over range $\sum_{k=1}^{N_k} P_{k,m}$ shown in panel B of Fig. 4. Ignoring the effect of the waveform image boundaries, its noise autocovariance function is given as

$$\begin{aligned} C_{\sum P}(x) &\approx \mathbb{E}\left[\sum_k \rho_{k,0}\sum_{k'}\rho_{k',m}\right] = \sum_k\sum_{k'}\mathbb{E}\left[\rho_{k,0}\rho_{k',m}\right] \\ &= \sum_k\sum_{k'} C_{\rho\ k-k',m} \approx N_k\sum_k C_{\rho\ k,m} \\ &\approx \mathcal{C}\int_{-\infty}^{\infty} C_\rho(r,x)\mathrm{dr} = \mathcal{C}\mathrm{sinc}^2(x/L_x). \end{aligned} \tag{28}$$

Therefore, by summing all range bins the range offset r_b in Eq. 27 has no effect on the outcome anymore and the noise ACF $R_{\sum P}(x)$ becomes indeed $\mathrm{sinc}^2(x/L_x)$. The waveform image data suffers from the effect of boundaries, hence small differences of about 0.05 between model and data are present. This example illustrates that one cannot directly make statements about the noise autocorrelation functions of the estimated SSH, SWH and sigma0 based on the behavior in Fig. 4A, because the estimates are obtained from the full waveform and not from the power variations along individual range gates.

3.3. Measured noise autocorrelation of geophysical estimates

While the noise ACFs of the waveform power and the cumulated waveform power in Fig. 4A,B showed no obvious sea state dependence, this is not the case for the noise ACFs of SSH and SWH estimates, see panels C–E. There are a few important observations to make. First of all, the SSH obtained from a threshold retracker and the SSH obtained from a SAMOSA2-based retracker present very different noise ACFs, and the former shows the faster decorrelation. On top of that, the SAMOSA2-based results show a significant sea state dependence, as the noise ACFs vary by up to 0.2 in the significant wave height range of 0–3 m. This sea state dependence is even more pronounced for the SWH estimates, where the ACFs vary by up to 0.3. Thus, although the SSH and SWH are obtained by the same retracker, they show different decorrelation

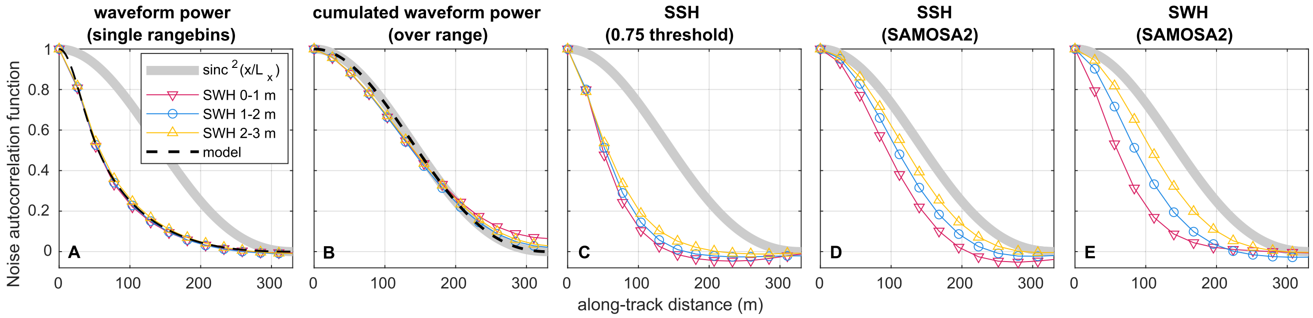

Fig. 4. Measured noise ACFs of different variables and for all Sentinel-3B overpasses, averaged in groups of SWH (upside down triangles, circles, triangles). The function $\mathrm{sinc}^2(x/L_x)$ (solid grey line) is shown as a reference in all panels. Panel A shows the speckle noise ACF along a fixed range rate, together with the model (Eq. 27, dashed line). Panel B shows the noise ACF of the cumulated power over range of the waveform image, in line with the model (Eq. 28, dashed line). Panels C and D provide the noise ACFs of the retracked SSH from a threshold retracker (0.75 threshold) and the SAMOSA2 retracker, respectively, and panel E provides the noise ACF of the retracked SWH from the SAMOSA2 retracker. 180 Doppler beams were used for multilooking within the UFSAR processing.

behavior. In the considered dataset it holds that, the calmer the sea state, the narrower the noise ACF of the geophysical estimates. We can conclude that.

- The along-track noise ACF of the geophysical estimates is heavily dependent on the chosen retracker.
- The along-track noise ACF of different geophysical estimates from the same retracker are different.
- The along-track noise ACF of different geophysical estimates may show a significant sea state dependence.

3.4. Model for the noise autocorrelation of geophysical estimates

The model for the speckle noise ACF in Eq. 27 is the first step towards modeling the behavior of the noise ACFs of SSH and SWH in Fig. 4. Modeling these requires to propagate the uncertainties and covariances of the waveform image through the retracking process, which yields the parameter estimates and which is different for each retracker. Since we are only interested in propagating the noise and not the underlying signal, we will assume in the remainder of this section a waveform image without variations of the mean $\mathbb{E}[P(\boldsymbol{r})]$ in along-track direction without loss of generality. For a (weighted) nonlinear least squares fit we require to characterize first the waveform image uncertainties up to a factor. The following derivations are split into the three steps of.

1. expressing the waveforms covariances for a real waveform image,
2. propagating the speckle noise through the retracking into the parameter estimates,
3. calculating explicitly the noise ACFs of estimated parameters.

The considerations in the previous section presume a constant power over the waveform image, which is not generally true. Using again that the speckle noise standard deviation is proportional to the mean, we approximate the covariance (Eq. 5) between any two points in the waveform image as

$$C_\rho(\boldsymbol{r}_1,\boldsymbol{r}_2) \approx \mathcal{C}\mathbb{E}[P(\boldsymbol{r}_1)]\mathbb{E}[P(\boldsymbol{r}_2)]R_\rho(\boldsymbol{r}_2-\boldsymbol{r}_1). \tag{29}$$

with numeric factor $\mathcal{C}$ dependent on the number of Doppler beams used for multilooking. In lack of the true mean $\mathbb{E}[P(\boldsymbol{r}]$ one can potentially use e.g. the value from the waveform image itself, a suitable moving average or median, or the smooth fit from a physical waveform model, all offering different advantages and disadvantages. Since the data is discrete, we continue rewriting Eq. 29 in the discrete form $C_{\rho\ k,k',m,m'}$, where k,m and k',m' are the indices to locations $\boldsymbol{r}_1$ and $\boldsymbol{r}_2$, respectively:

$$C_{\rho\ k,k',m,m'} = \mathcal{C}\mathbb{E}[P_{k,m}]\mathbb{E}\left[P_{k',m'}\right]R_{\rho\ k-k',m-m'} \tag{30}$$

Using that the mean power is not changing in along-track direction ($\mathbb{E}[P_{k,m}] = \mathbb{E}[P_k]$ for all m) we can simplify to

$$C_{\rho\ k,k',m,0} = \mathcal{C}\mathbb{E}[P_k]\mathbb{E}[P_{k'}]R_{\rho\ k-k',m}. \tag{31}$$

In a second step we consider the retracking. Here, in line with EUMETSAT (2021) we assume it is performed via a non-linear least squares estimation using a column vector $\boldsymbol{P} = P_k$ of the waveform image $P_{k,m}$. Hence, we minimize the two-norm of the differences

$$||\boldsymbol{P} - \boldsymbol{P}^{\text{model}}(\boldsymbol{\beta})||_2 \tag{32}$$

for the parameter vector $\boldsymbol{\beta}$ of the waveform model $\boldsymbol{P}^{\text{model}}$, which typically contains epoch, SWH and Pu. Linearization around the true parameter values $\boldsymbol{\beta}^*$ yields

$$||\boldsymbol{P} - \boldsymbol{P}^{\text{model}}(\boldsymbol{\beta}^*) - \mathbf{J}\boldsymbol{\epsilon}_\beta||_2, \tag{33}$$

with the Jacobian matrix $\mathbf{J} = J_{kj} = \partial P_k^{\text{model}}(\boldsymbol{\beta}^*)/\partial\beta_j$ of the waveform model and the difference $\boldsymbol{\epsilon}_\beta = \boldsymbol{\beta} - \boldsymbol{\beta}^*$ between the estimated parameters and the true ones (hence the estimates' noise). Since the waveform model is typically a model of the mean power (e.g. Ray et al., 2015; Dinardo, 2020), we approximate the true mean $\mathbb{E}[\boldsymbol{P}]$ with the model evaluated at the correct parameters and obtain

$$||\boldsymbol{\rho} - \mathbf{J}\boldsymbol{\epsilon}_\beta||_2, \tag{34}$$

with $\boldsymbol{\rho} = \rho_k$ the respective column of the speckle noise image $\rho_{k,m}$. This linear least squares problem has the well known analytical solution

$$\boldsymbol{\epsilon}_\beta = (\mathbf{J}^\intercal\mathbf{J})^{-1}\mathbf{J}^\intercal\boldsymbol{\rho} = \mathbf{W}\boldsymbol{\rho} \tag{35}$$

where the Jacobian defines the weighting matrix $\mathbf{W} = (\mathbf{J}^\intercal\mathbf{J})^{-1}\mathbf{J}^\intercal$. It has to be stressed that if another approach than least squares minimization (e.g. weighted least squares) is followed instead, then the expression for $\mathbf{W}$ would need to be modified accordingly. It follows from Eq. 35 that the noise of the estimated variables can be written as a weighted sum of the speckle noise values. This becomes clearer when writing out the rows of $\mathbf{W}$ explicitly

$$\begin{pmatrix} \epsilon_{\text{epoch}} \\ \epsilon_{\text{SWH}} \\ \epsilon_{\text{Pu}} \end{pmatrix} = \begin{pmatrix} \boldsymbol{W}^\intercal_{\text{epoch}} \\ \boldsymbol{W}^\intercal_{\text{SWH}} \\ \boldsymbol{W}^\intercal_{\text{Pu}} \end{pmatrix} \boldsymbol{\rho}, \tag{36}$$

with the weighting vectors $\boldsymbol{W}_{\text{estimate}}$ of the same length as $\boldsymbol{\rho}$, meaning that the estimates' noise can be obtained from the scalar product (or weighted sum)

$$\epsilon_{\text{estimate}} = \boldsymbol{W}_{\text{estimate}} \cdot \boldsymbol{\rho} = \sum_k W_{\text{estimate}\ k}\rho_k. \tag{37}$$

Using this in a third step, the noise autocovariance function of a parameter estimate ϵ in along-track direction can be explicitly written as

$$C_{\epsilon\ m} = \mathbb{E}[\epsilon_0\epsilon_m] = \mathbb{E}\left[\sum_k W_k\rho_{k,0}\sum_{k'} W_{k'}\rho_{k',m}\right]$$

$$= \sum_k\sum_{k'} W_k W_{k'}\mathbb{E}\left[\rho_{k,0}\rho_{k',m}\right]. \tag{38}$$

Replacing the autocovariance function of the waveform image speckle noise $\mathbb{E}\left[\rho_{k,0}\rho_{k',m}\right]$ with Eq. 31 yields

$$C_{\epsilon\ m} = \mathcal{C}\sum_k W_k\mathbb{E}[P_k]\sum_{k'} W_{k'}\mathbb{E}[P_{k'}]R_{\rho\ k-k',m} \tag{39}$$

$$\approx \mathcal{C}\sum_k W_k P_k^{\text{model}}(\boldsymbol{\beta}^*)\sum_{k'} W_{k'}P_{k'}^{\text{model}}(\boldsymbol{\beta}^*)R_{\rho\ k-k',m}. \tag{40}$$

In the last step we approximated the true mean of the waveform image with the physical waveform model that is used for retracking, evaluated at the true parameter values. Mathematically speaking, the result is the scalar product of $W_k P_k^{\text{model}}$ with the convolution of $W_k P_k^{\text{model}}$ and $R_{\rho\ k,m}$. The noise autocorrelation function $R_{\epsilon\ m} = R_\epsilon(x)$ of the estimates is then obtained by proper normalization (choice of $\mathcal{C}$). The modelled noise ACFs $R_{\text{Pu}}, R_{\text{epoch}}$ and R_{SWH} are plotted in Fig. 5 using a SAMOSA2 model to obtain both P_k^{model} and W_k (the latter is dependent on the models' derivatives as underlined above). It needs to be stressed, that for an arbitrary retracker one will always need to obtain W_k from the Jacobian of the retracker itself, while P_k^{model} should be obtained from the most accurate available representation of the mean waveform image, e.g. preferably a numerical model such as in Buchhaupt et al. (2018). In lack of such a numerical model, we use the physical SAMOSA2 model for both. From Eq. 40 we can conclude that

- the noise ACF of the retracked parameters inherits all dependencies from the physical waveform model (and/or retracker), including all Level-2 processing parameters and the satellites' roll and pitch mispointing,
- particularly, the noise ACF of all parameter estimates is itself strongly sea state dependent.

Assuming that the epoch and sigma0 only change the relative position of the waveform and its amplitude, respectively (compare to Ray et al., 2015), but leave its shape

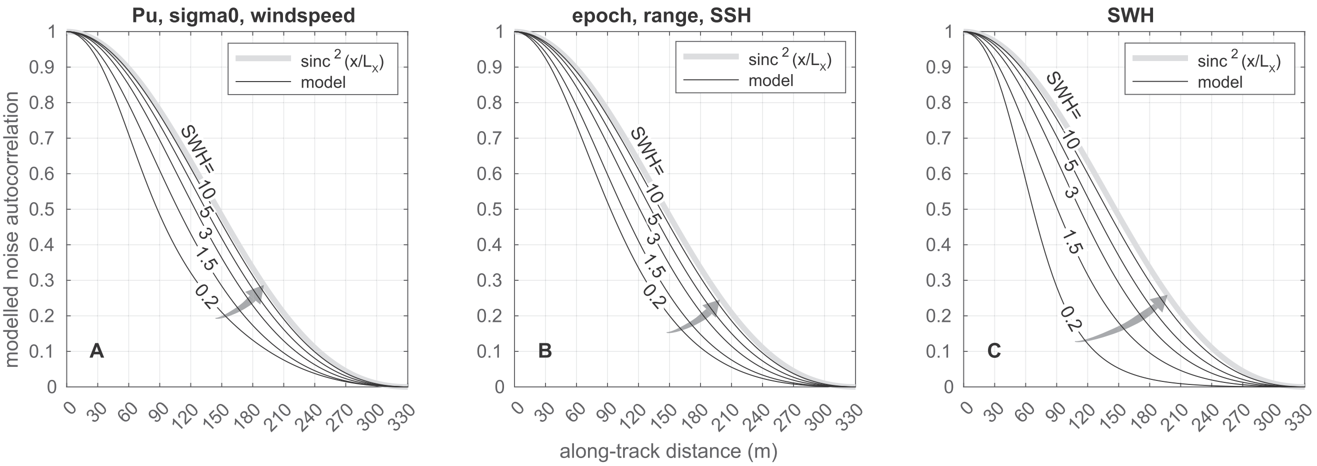

Fig. 5. Modeled noise ACFs of SAMOSA2-retracked parameters of Sentinel-3B according to Eq. 40 at different SWH (in m) and for multilooking of 180 Doppler beams. In line with the data in Fig. 4, the model predicts a swifter decorrelation than anticipated by the UFSAR PTR (Eq. 2).

almost untouched, their dependence can be ignored. Therefore, the sea state dependence expresses itself mainly by significant wave height, which is illustrated in Fig. 5. The model reproduces the sea state dependence seen in the data, when compared to Fig. 4 D–E. In line with the data, it predicts that the SWH noise generally decorrelates faster than the noise of SSH and sigma0 for low sea states. On the other hand, all noise ACFs converge towards $\mathrm{sinc}^2(x/L_x)$ with increasing SWH. In essence, increasing SWH widens the waveform in range direction, so that $W_k P_k^{\mathrm{model}}$ itself becomes smoother. Therefore, the noise ACF of all estimates starts resembling the noise ACF of the cumulated waveform power over range (compare to Eq. 28), which explains the increasing resemblance with $\mathrm{sinc}^2(x/L_x)$.

To assess the model's performance, the obtained SSH noise ACF model from Eq. 40 is compared to the Sentinel-3B data in Fig. 6. Each overpass corresponds to a different sea state, therefore, each overpass is considered individually. The analysis demonstrates that modeling the SSH noise ACF simply as $\mathrm{sinc}^2(x/L_x)$ is inappropriate in general. In this case, absolute differences as high as 0.6 can be observed and the root mean square error (RMSE) is 0.3 over the considered dataset. Using our model improves this situation significantly, particularly when feeding it with the median SWH of each overpass. In that case, the RMSE between modelled and measured ACF reduces to 0.046. This value resembles a conservative upper limit for the model error, since this estimation includes the uncertainties from the empirically obtained SSH noise ACFs themselves.

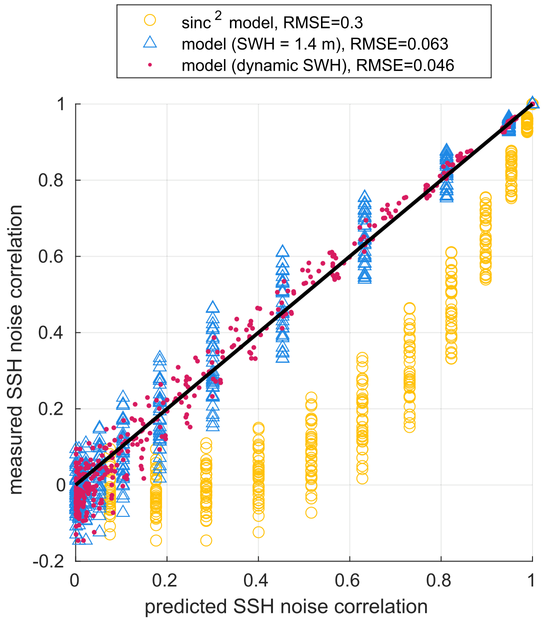

Fig. 6. Comparison of the measured SAMOSA2 SSH noise ACFs from Fig. 4D with different models: Assuming $R_{\mathrm{SSH}} = \mathrm{sinc}^2(x/L_x)$ (yellow circles); Using our model (Eq. 40, Fig. 5) with the median SWH of all overpasses (blue triangles); Using our model (Eq. 40) with the median SWH per overpass (red dots). The black line marks perfect agreement. All data points with along-track lags of less than 320 m are considered.

The noise ACF is linked to the noise power spectral density (PSD) via Fourier transform (Wiener-Kintchin theorem), so we can estimate as well the noise PSD. Fig. 7 shows the modeled noise PSD of sigma0, SSH and SWH for an SWH of 1 m. As before, the limiting case $R = \mathrm{sinc}^2(x/L_x)$ is shown as a reference, its corresponding PSD is a triangular function. This PSD falls below the −20 dB threshold (below 1% of its maximum) at a frequency (posting rate equivalent) of 20 Hz. As discussed in the introduction already, this requires a minimum posting rate of 40 Hz according to the Nyquist limit. In general, the noise PSDs of sigma0, SSH and SWH are wider than this reference. They fall below the −20 dB threshold around 40 Hz for sigma0 and SSH, and 50 Hz for SWH. This indicates that posting rates around 80 and 100 Hz are necessary to sample the noise in an unaliased manner. These sampling requirements become even stricter for SWH below 1 m. In practice however, these calm sea states are often associated to specular echoes due to a small mean square slope of the ocean surface (see e.g. Dinardo et al., 2021), in which case our model (Eq. 40) reduces to the limiting case of $R = \mathrm{sinc}^2(x/L_x)$. The same holds for specular waveform echoes over rivers. This means that our ACF model is most useful over comparably rough surfaces like oceans and potentially sea ice.

Finally, we can conclude that the behavior observed in Fig. 4 is well explained by our model and is in line with the earlier works on this topic (Dinardo et al., 2015; Buchhaupt, 2019; Egido et al., 2021; Rieu et al., 2021b). However, we need to add two remarks regarding the methodology. The first is about the interpretation of an increased Effective Number of Looks (ENL) with posting rate, the second about the arithmetic mean for subsampling.

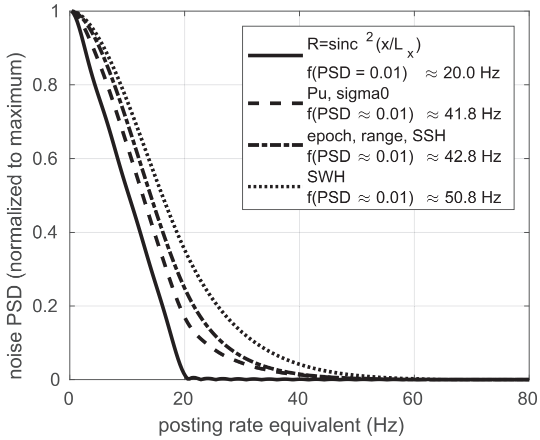

Fig. 7. Modelled noise PSDs of retracked parameters according to Eq. 40 at SWH = 1 m. The noise PSDs are obtained from the noise ACFs by Fourier transform (Wiener-Kintchin Theorem). The legend indicates the frequency at which the noise PSDs fall below a 1% threshold (−20 dB). The limiting case of $R = \mathrm{sinc}^2(x/L_x)$ is shown as reference.

Interpretation of the Effective Number of Looks (ENL)

The ENL is a helpful metric to characterize the relative noise in a waveform image. But this metric is calculated from the waveform power along a single range gate (see Fig. 4A). Because this property decorrelates differently than the retracked parameters (see Fig. 4C–E), care must be taken when interpreting an increasing of ENL with posting rate. This increase will not reflect the behavior of the retracked parameters.

Sub-sampling of retracked parameters from 80 Hz to 20 Hz with arithmetic mean

Dinardo et al. (2015), Rieu et al. (2021b) and Egido et al. (2021) suggest to sub-sample the parameter estimates obtained on 80 Hz by applying an arithmetic mean. While the data is truly uncorrelated at 20 Hz steps (~320 m), we have shown that this is not the case for the data at 80 Hz (~80 m, see Fig. 5). Therefore, the arithmetic mean is no longer the optimal estimator (in terms of minimal variance). The hidden consequence of sub-sampling by arithmetic averaging in presence of non-trivial correlations is, that it introduces correlation between the consecutive sub-sampled 20 Hz estimates, while the original 20 Hz samples are uncorrelated, see Fig. 8. This implies that a part of the noise reduction with respect to the original 20 Hz data (see Fig. 8 and Dinardo et al. (2015), Egido et al. (2021)) is caused by inordinate low-pass filtering, and hence spurious. To elaborate on this point, imagine a random white noise process. By application of a moving mean we may suppress the noise, but simultaneously introduce sample-to-sample correlation. Hence, in this example the apparent noise reduction was merely caused at the price of increased correlation length, but not by exploiting additional, independent information. This causes that the reported precision gains might be too optimistic. Assuming Gaussian noise with autocorrelation function $\mathrm{sinc}^2(x/L_x)$ and sampling according to $L_x/4$ (80 Hz equivalent) it can be shown that the outlined averaging to 20 Hz results in 19% spurious precision gain, while increasing the sample-to-sample correlation from 0 to 0.19. Though we are certain that the parameters' precision can be significantly improved with respect to the 20 Hz sampling due to the narrower noise ACFs (see Fig. 5), a proper quantification of the improvements remains because of the aforementioned reasons. Fairly assessing the gain in parameter precision with posting rate requires an optimal filter for 20 Hz sub-sampling. Such filter needs to minimize noise variances while avoiding spurious sample-to-sample correlations for comparability to the original product. Necessary input to such a filter is the noise ACF model developed here.

4. Discussion

In this work we have implicitly made use of some common approximations, which will have a small influence on the ACF model. (i) We have modeled the antenna gain pattern with a Gaussian function and the PTR as a sinc^2-function (Ray et al., 2015; Dinardo, 2020; Dinardo et al., 2021; Rieu et al., 2021a). In principle, one can use more advanced formulations of the antenna gain pattern (e.g. Wingham et al., 2004; Scagliola et al., 2015b) or empirically determined functional shapes of the PTR (e.g. Mertikas et al., 2020; Abileah and Vignudelli, 2021), so that any degree of detail can be incorporated into the ACF model. (ii) Furthermore, we have assumed a flat earth approximation, which causes small deviations (smaller than 0.03) in the 2D speckle noise ACF model Eq. 27. As the noise ACF of the retracked estimates is the result of a convolution (see Eq. 40), which typically balances out positive and negative deviations, the impact on the estimates' noise ACFs is generally smaller. (iii) In the derivations above we

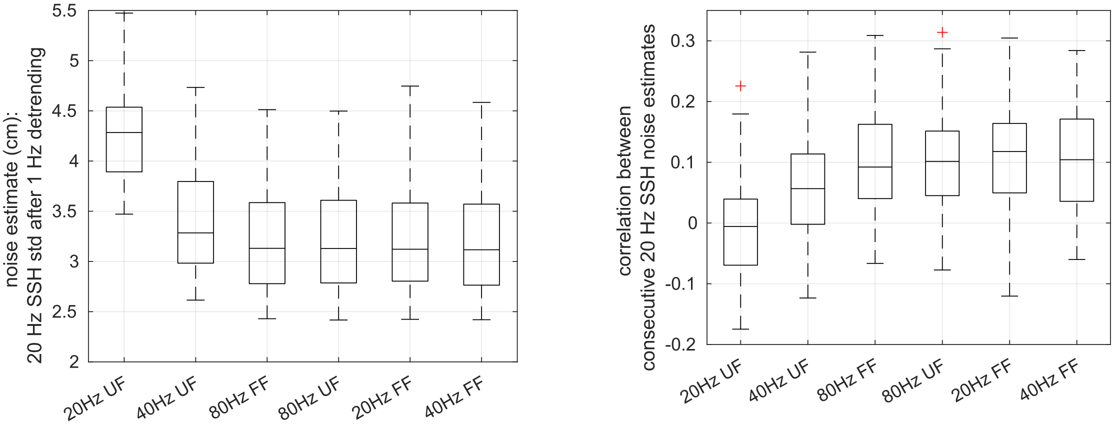

Fig. 8. Influence of subsampling to 20 Hz for UFSAR (marked as UF) and FFSAR (marked as FF) on 20 Hz noise SSH noise standard deviation (left) and sample-to-sample correlation (right) for all Sentinel-3B overpasses. Each boxplot is obtained from all 36 overpasses. The retracking is performed with multilooked waveforms at 20, 40 and 80 Hz and the same SAMOSA2 models for UFSAR and FFSAR as in Ehlers et al. (2022). After that, the SSH is subsampled onto 20 Hz by taking an arithmetic mean of the nearest 40 Hz and 80 Hz samples (Dinardo et al., 2015; Rieu et al., 2021b; Egido et al., 2021), after which the 20 Hz noise standard deviation and sample-to-sample correlation is calculated. The sampling configurations that indicate highest precision suffer from increased sample-to-sample correlation, rendering the comparison with UFSAR at 20 Hz posting rate unfair.

have assumed that the backscatter cross section sigma0 is not dependent on incidence angle (rough surface approximation). If not constant, σ_0 is commonly modeled with Gaussian dependence for small incidence angles (Brown, 1977; Dinardo, 2020; Buchhaupt et al., 2021), whose width relates to the mean square sea surface slope (Valenzuela, 1978; Brown, 1977). As such, it can be split into $\sigma_0(x,y) = \sigma_{0,x}(x)\sigma_{0,y}(y)$ and absorbed into the antenna pattern. This means, one simply replaces $G_i^2(i)$ with $G_i^2(i)\sigma_{0,i}(i)$ for $i = x, y$. However, the mean square slope is an additional free parameter that must be prescribed beforehand, for example by the range integrated power of a Doppler beam stack, as described in Dinardo et al. (2021). This dependence becomes particularly important for small significant wave height (e.g. below 1 m) and has not been explicitly modelled here. Generally, the influence of changing mean square slope is comparable to the influence of changing the number of Doppler beams for multilooking, as shown in Fig. 3.

We have assumed stationary speckle noise within the waveform image, see Eq. 7. It was shown by Moreau et al. (2018), Rieu et al. (2021b), Collard et al. (2022), Altiparmaki et al. (2022) that the UFSAR and FFSAR waveform images are also sensitive to the presence of swell waves. This causes that the expected power $\mathbb{E}[P(\boldsymbol{r})]$ is effectively varying in an harmonic fashion on small scales, violating the assumption of ergodicity (stationarity). While the definition Eq. 7 and the assumptions on the speckle noise distribution itself will remain true, $\mathbb{E}[P(\boldsymbol{r})]$ is not constant in along-track direction as presumed and therefore one cannot exchange an along-track moving mean to estimate the ensemble mean, i.e. these swell-induced variations will inevitably contribute when trying to estimate the speckle noise ACF empirically as in Section 2.6.2. Therefore, we need to make a clear distinction between the “noise” caused by speckle and the “noise” caused by swell waves, as our model describes only the former. The noise ACF model can only be extended for this contribution once a forward model is developed that describes the altimeter observations in presence of swell (see the discussion in Altiparmaki et al., 2022). A first step will be to validate the here developed noise ACF model depending on swell presence to assess its sensitivity. However, already now we have explained why the posting rates that are required for unaliased sampling may generally reach up to 100 Hz, depending on the desired parameter, the retracker and the sea state conditions (see Fig. 7).

Related to the last paragraph is the effect of sea surface motion on the UFSAR processing discussed in Buchhaupt (2019), Buchhaupt et al. (2021). The vertical velocity of the sea surface causes that scatterers appear mislocated within the waveform image with respect to the assumption of a sea surface at rest. Due to the blur caused by vertical velocity variance, the mean power $\mathbb{E}[P(\boldsymbol{r})]$ in the waveform image will generally not vary on along-track length scales lower than 50–100 m, irregardless of whether UFSAR or FFSAR methods are being used. This effect is also referred to as azimuth cutoff in SAR literature (Vachon et al., 1994; Kerbaol et al., 1998). However, in scenes with little visual contrast, as is the case for the altimeter waveforms, the along-track (azimuthal) ACF still resembles closely the point spread function associated with the speckle noise, and the cutoff-related term is typically magnitudes smaller (see e.g. Fig. 9a in Kerbaol et al., 1998). Therefore, the effect of velocity variance can be understood as an incorrect mapping to the sea surface, rather than changing the properties of the waveforms' speckle ACF directly.

5. Conclusions

The UFSAR altimetry signal is typically sampled at along-track intervals $L_x \approx 320$ m corresponding to the theoretical Doppler frequency resolution, which resembles close to 20 Hz sampling for Sentinel-3, CryoSat-2 and Sentinel-6 Michael Freilich. In this work we discussed the difference between the along-track noise decorrelation and the resolution of the Delay-Doppler processed SAR altimeter data. We stress that it is important to consider the noise autocorrelation function (statistical dependence) to leverage maximum precision and to obtain unaliased along-track spectra, rather than the resolution L_x. We then derived a model for the noise ACF of the speckle in the waveform image and the retracked parameters such as sigma0, SSH and SWH and show that they generally decorrelate over distances shorter than the theoretical Doppler resolution L_x. A performance check with Sentinel-3B data shows that our noise ACF model reproduces the empirical SSH noise ACF with an RMSE of less than 0.05. Thereafter, we demonstrate for the first time that the modeled noise PSDs may contain frequencies up to 50 Hz, requiring up to 100 Hz posting rate for unaliased sampling. Interestingly, the required posting rate is highly variable between 40–100 Hz, because the noise ACF and noise PSD of a retracked parameter strongly depend on (i) the applied retracker (waveform model), (ii) the kind of retracked variable itself and (iii) the sea state (particularly the SWH). On top of that, noise ACF and noise PSD of a retracked parameter depend on all Level-1b processing parameters, particularly on (iv) antenna gain pattern compensation and windowing and (v) the number of Doppler beams used for multilooking. Regardless of sea state and the number of Doppler beams used, we find that the required posting rate is always higher than or equal to 40 Hz (equivalent to ground distances of $L_x/2$). The revelation of these dependencies and their consequences for the UFSAR posting rate is the main novelty of this work.

Overall, our results are in accordance to earlier work on the topic (Dinardo et al., 2015; Buchhaupt, 2019; Egido et al., 2021; Rieu et al., 2021b). Particularly, we can confirm that the highest precision gain is expected for calm sea states (low SWH, see Egido et al., 2021), which implies improvements in vicinity to the coasts. Furthermore, we confirm that a 20 Hz posting rate implies undersampling of the UFSAR measurements. However, we have also noticed that the earlier reported precision improvements of 40 and 80 Hz with respect to default 20 Hz data of up to 35% may have been too optimistic due to application of the arithmetic mean to correlated data. Therefore, the possible precision gain offered by higher posting rates remains to be fairly quantified. Necessary input to this assessment is the noise ACF model developed here, which can be tuned to different SAR altimeter missions and processing settings.

Apart from the aforementioned points, our noise ACF model can also be used to apply optimal estimation filters (such as a Kalman-filter) to UFSAR measurements or for proper sub-sampling. The model may also be extended straightforwardly to predict the sea state dependent noise cross-covariance functions between different retracked variables. This is of interest, because non-zero noise cross-covariance between retracked variables allows for an additional noise variance reduction of SSH (Garcia et al., 2014; Zaron and deCarvalho, 2016; Tran et al., 2021, and references therein). Furthermore, the model of the noise PSD will facilitate to distinguish small scale physical processes from noise in the power spectra of e.g. sea level anomaly in along-track direction. In combination with the highest expected precision gain in calm sea states – typical in vicinity of the coasts – our results may benefit studies of small scale coastal processes in particular. The developed model may also aid studies regarding advanced image processing of UFSAR waveforms e.g. related to swell detection, as already performed for FFSAR by Altiparmaki et al. (2022).

In order to apply our noise ACF model to estimates from another retracker, one needs to consider only Eq. 40 and Eq. 27, together with a waveform model and/or the retracker of choice. That applies in case no additional windowing is used in the UFSAR processing

Declaration of Competing Interest

The authors declare that they have no known competing financial interests or personal relationships that could have appeared to influence the work reported in this paper.

Acknowledgments

This research was supported by the Nederlandse Organisatie voor Wetenschappelijk Onderzoek (NWO) under Grant No. ALWGO.2019.016.

Appendix A. Simplifying the speckle noise autocovariance function

In this Appendix we plug Eq. 17 into Eq. 16 and use the Assumptions 19, 20 to simplify the result. In the remainder of this Appendix we drop the subscript b, though all variables refer to a specific burst. The problem contains a transfer function (PTR) that is two-dimensional, and a noise that is complex-valued. We will assume here that the PTR is separable into $h(\boldsymbol{r}) = R(r)X(x)$ (this is not the case for h_b in Eq. B.2, but it can be made separable with an area-conserving variable transform, which will be discussed later on). Since also the real and imaginary part of the true return echo ε are statistically independent, we will here sketch only the derivation for the one-dimensional case $h(\boldsymbol{r}) = X(x)$ with a real-valued noise $\varepsilon = \eta$, which readily generalizes to the two-dimensional case with complex-valued noise when accounting for a factor of 2. As before, we use indices m for the along-track distance $x = m\Delta x$. Using Eq. 17, the first term of the right hand side of Eq. 16 can be written out as a quadruple product of convolutions

$$\mathbb{E}[P(0)P(x)] = \mathbb{E}\Bigg[\sum_{m'} X_{m'}\eta_{0-m'}\sum_{m''} X_{m''}\eta_{0-m''}\cdots \tag{A.1}$$

$$\sum_{m'''} X_{m'''}\eta_{m-m'''}\sum_{m''''} X_{m''''}\eta_{m-m''''}\Bigg] \tag{A.2}$$

$$= \sum_{m',\ldots,m''''} X_{m'}\cdots X_{m''''}\,\mathbb{E}[\eta_{0-m'}\eta_{0-m''}\eta_{m-m'''}\eta_{m-m''''}]. \tag{A.3}$$

where distributivity of the sum and linearity of the expectation have been used in the last step. This expression contains the fourth order statistic $\mathbb{E}[\eta_m\eta_n\eta_o\eta_p]$ of the speckle noise, which in most cases is equal to zero because η is assumed spatially white. However, it is not zero, when either all four indices are identical or when pairs of indices are identical simultaneously (the other cases give no contribution because of the zero mean of η). Since the first case includes the others, we have to account for double-counting and can write

$$\begin{aligned}\mathbb{E}[\eta_m\eta_n\eta_o\eta_p] = {} & (K\sigma^4 - 3\sigma^4)\delta_{m,n}\delta_{n,o}\delta_{o,p} \\ & + \ldots \sigma^4\delta_{m,n}\delta_{o,p} + \sigma^4\delta_{m,o}\delta_{n,p} \\ & + \sigma^4\delta_{m,p}\delta_{n,o},\end{aligned} \tag{A.4}$$

with kurtosis K of the distribution of η and Kronecker-delta $\delta_{m,n}$. Since $K = 3$ for a normal distribution, the first term vanishes. Inserting this back into the quadruple sum, using the sifting property of the Kronecker-delta, symmetry of the PTR X_m and simplifying eventually yields

$$\mathbb{E}[P(0)P(x))] = 2\sigma^4|(h*h)(x)|^2 + \mathbb{E}[P(0)]\mathbb{E}[P(x)], \tag{A.5}$$

which generalizes to

$$\mathbb{E}[P(0)P(\boldsymbol{r}))] = 4\sigma^4|(h*h)(\boldsymbol{r})|^2 + \mathbb{E}[P(0)]\mathbb{E}[P(\boldsymbol{r})] \tag{A.6}$$

in the two-dimensional case with complex-valued true return signal ε. Therefore we get that Eq. 16 becomes

$$\mathbb{E}[\rho(0)\rho(\boldsymbol{r})] = 4\sigma^4|(h*h)(\boldsymbol{r})|^2 \tag{A.7}$$

under the condition that h is separable.

Appendix B. Derivation of the multilooked PTR

In line with Ray et al. (2015) we choose a local coordinate system with along-track distance x, cross-track distance y, and height z, centered on the Earth's surface. Using all provided definitions and zero surface curvature ($\alpha = 1$, flat Earth approximation) one can verify in Eq. 2 that

$$k - k_l = \frac{2B}{c}\left[r + z - \frac{x^2}{2H} - \frac{y^2}{2H} + \frac{(lL_x)^2}{2H}\right], \tag{B.1}$$

where the last term guarantees that the leading edge falls into the same range bin across all Doppler beams. Eq. 2 represents the Doppler beams pointing from one burst towards different ground positions. Assuming a constant satellite velocity over the illumination time, the problem becomes translational invariant, i.e. steering a Doppler beam from a burst at time $t_b = 0$ to an along-track position $x = lL_x$ is the same as steering a Doppler beam from a burst at time $t_b = -lL_x/V$ to position $x = 0$. Since only the inverse of the satellite's elevation H appears in the equation, its changes on the order of several meters within the synthetic aperture may be ignored as well compared to several hundred kilometers altitude. Given the burst timings $t_b \in [-T_\mathrm{m}/2, T_\mathrm{m}/2]$, all non-integer Doppler beams with $x_l = L_x l = Vt_b$ contribute to the multilooked UF-SAR waveform. So in order to describe the Doppler beam contribution from a burst b at time t_b steered to the ground location $x = 0$, we apply the variable transformation $x \rightarrow x + Vt_b$ in Eq. 2 and use Eq. B.1, which yields for the PTR power from burst b

$$\tilde{h}_b^2(r,x) \approx \mathcal{C}\mathrm{sinc}^2\left[\frac{x}{L_x}\right]\mathrm{sinc}^2\left[\frac{2B}{c}\left(r + z - \frac{x^2}{2H} - \frac{y^2}{2H} - \frac{xVt_b}{H}\right)\right], \tag{B.2}$$

where the tilde is used to make clear our change of perspective. Then, using that the Doppler beams are weighted with the azimuth antenna gain power pattern $G_x^2(x)$ the multilooked PTR power h_m^2 becomes

$$\begin{aligned} h_m^2 &\approx \sum_{t_b} G_x^2(Vt_b)\tilde{h}_b^2 \\ &\approx \mathcal{C}\mathrm{sinc}^2\left[\frac{x}{L_x}\right]\sum_{t_b} G_x^2(Vt_b)\mathrm{sinc}^2\left[\frac{2B}{c}\left(r + z - \frac{x^2}{2H} - \frac{y^2}{2H} - \frac{xVt_b}{H}\right)\right]. \end{aligned} \tag{B.3}$$

Now, the only remaining difference to Eq. 3 is the (small) term $xf_cV(Hs)^{-1}$ that we include to account for the additional apparent range shift due to the Doppler effect. For the antenna pattern we apply

$$G_x^2(x) = \exp\left(-\gamma_x\theta_\mathrm{look}^2(x)\right) \tag{B.4}$$

in line with Dinardo (2020) and using

$$\gamma_x = 8\ln(2)/\theta_x \quad \text{and} \quad \theta_\mathrm{look}(x = Vt_b) \approx Vt_b/H. \tag{B.5}$$

References

Abileah, R., Vignudelli, S., 2021. Precise inland surface altimetry (PISA) with nadir specular echoes from Sentinel-3: Algorithm and performance assessment. Remote Sens. Environ. 264, 112580. https://doi.org/10.1016/j.rse.2021.112580, URL: https://www.sciencedirect.com/science/article/pii/S003442572100300X.

Altiparmaki, O., Kleinherenbrink, M., Naeije, M., et al., 2022. SAR Altimetry Data as a New Source for Swell Monitoring. Geophys. Res. Lett. 49 (7). https://doi.org/10.1029/2021GL096224, e2021GL096224, URL: https://onlinelibrary.wiley.com/doi/abs/10.1029/2021GL096224. _eprint: https://onlinelibrary.wiley.com/doi/pdf/10.1029/2021GL096224.

Brown, G., 1977. The average impulse response of a rough surface and its applications. IEEE Trans. Antennas Propag. 25 (1), 67–74. https://doi.org/10.1109/TAP.1977.1141536, Conference Name: IEEE Transactions on Antennas and Propagation.

Buchhaupt, C., 2019. Model Improvement for SAR Altimetry. Ph.D. thesis Technische Universität Darmstadt. URL: http://oatd.org/oatd/record?record=oai%5C%3Atuprints.ulb.tu-darmstadt.de%5C%3A9015.

Buchhaupt, C., Fenoglio, L., Becker, M., et al., 2021. Impact of vertical water particle motions on focused SAR altimetry. Adv. Space Res. 68 (2), 853–874. https://doi.org/10.1016/j.asr.2020.07.015, URL: https://linkinghub.elsevier.com/retrieve/pii/S0273117720304920.

Buchhaupt, C., Fenoglio-Marc, L., Dinardo, S., et al., 2018. A fast convolution based waveform model for conventional and unfocused SAR altimetry. Adv. Space Res. 62 (6), 1445–1463. https://doi.org/10.1016/j.asr.2017.11.039, URL: https://www.sciencedirect.com/science/article/pii/S0273117717308505.

Collard, F., Marié, L., Nouguier, F., et al., 2022. Wind-Wave Attenuation in Arctic Sea Ice: A Discussion of Remote Sensing Capabilities. J. Geophys. Res.: Oceans 127 (7). https://doi.org/10.1029/2022JC018654, e2022JC018654. URL: https://onlinelibrary.wiley.com/doi/abs/10.1029/2022JC018654. _eprint: https://agupubs.onlinelibrary.wiley.com/doi/pdf/10.1029/2022JC018654.

Dinardo, S., 2020. Techniques and Applications for Satellite SAR Altimetry over water, land and ice. Ph.D. Thesis Technische Universität Darmstadt. URL: https://tuprints.ulb.tu-darmstadt.de/11343/ iSBN: 9783935631457 Volume: 56.

Dinardo, S., Fenoglio-Marc, L., Becker, M., et al., 2021. A RIP-based SAR retracker and its application in North East Atlantic with Sentinel-3. Adv. Space Res. 68 (2), 892–929. https://doi.org/10.1016/j.asr.2020.06.004, URL: https://www.sciencedirect.com/science/article/pii/S0273117720304063.

Dinardo, S., Lucas, B., Benveniste, J., 2015. Coastal and inland water sar altimetry at 80 hz. In: 2015 Ocean Surface Topography Science Team (OSTST) Meeting.

Egido, A., Dinardo, S., Ray, C., 2021. The case for increasing the posting rate in delay/Doppler altimeters. Adv. Space Res. 68 (2), 930–936. https://doi.org/10.1016/j.asr.2020.03.014, URL: https://linkinghub.elsevier.com/retrieve/pii/S0273117720301691.

Egido, A., Smith, W.H.F., 2017. Fully focused SAR altimetry: theory and applications. IEEE Trans. Geosci. Remote Sens. 55 (1), 392–406. https://doi.org/10.1109/TGRS.2016.2607122, Conference Name: IEEE Transactions on Geoscience and Remote Sensing..

Ehlers, F., Schlembach, F., Kleinherenbrink, M., et al., 2022. Validity assessment of SAMOSA retracking for fully-focused SAR altimeter waveforms. Adv. Space Res. https://doi.org/10.1016/j.asr.2022.11.034, URL: https://www.sciencedirect.com/science/article/pii/S0273117722010651.

Engen, G., Johnsen, H., 1995. SAR-ocean wave inversion using image cross spectra. IEEE Trans. Geosci. Remote Sens. 33 (4), 1047–1056. https://doi.org/10.1109/36.406690, Conference Name: IEEE Transactions on Geoscience and Remote Sensing.

EUMETSAT, 2021. Sentinel-6/Jason-CS ALT Level 1 Product Generation Specification (L1 ALT PGS) — EUMETSAT. URL: https://www-cdn.eumetsat.int/files/.

Garcia, E.S., Sandwell, D.T., Smith, W.H., 2014. Retracking CryoSat-2, Envisat and Jason-1 radar altimetry waveforms for improved gravity field recovery. Geophys. J. Int. 196 (3), 1402–1422. https://doi.org/10.1093/gji/ggt469.

Gómez-Enri, J., Gommenginger, C.P., Srokosz, M.A., et al., 2007. Measuring Global Ocean Wave Skewness by Retracking RA-2 Envisat Waveforms. J. Atmosph. Oceanic Technol. 24 (6), 1102–1116. https://doi.org/10.1175/JTECH2014.1, URL: https://journals.ametsoc.org/view/journals/atot/24/6/jtech2014_1.xml. Publisher: American Meteorological Society Section: Journal of Atmospheric and Oceanic Technology.

Goodman, J.W., 1976. Some fundamental properties of speckle*. JOSA 66 (11), 1145–1150. https://doi.org/10.1364/JOSA.66.001145, URL: https://opg.optica.org/josa/abstract.cfm?uri=josa-66-11-1145. Publisher: Optica Publishing Group.

Jakeman, E., Pusey, P., 1976. A model for non-Rayleigh sea echo. IEEE Trans. Antennas Propagat. 24 (6), 806–814. https://doi.org/10.1109/TAP.1976.1141451, Conference Name: IEEE Transactions on Antennas and Propagation.

Kerbaol, V., Chapron, B., Vachon, P.W., 1998. Analysis of ERS-1/2 synthetic aperture radar wave mode imagettes. J. Geophys. Res.: Oceans 103 (C4), 7833–7846. https://doi.org/10.1029/97JC01579, URL: https://onlinelibrary.wiley.com/doi/abs/10.1029/97JC01579. _eprint: https://onlinelibrary.wiley.com/doi/pdf/10.1029/97JC01579.

Kleinherenbrink, M., Naeije, M., Slobbe, C., et al., 2020. The performance of CryoSat-2 fully-focussed SAR for inland water-level estimation. Remote Sens. Environ. 237, 111589. https://doi.org/10.1016/j.rse.2019.111589, URL: https://linkinghub.elsevier.com/retrieve/pii/S0034425719306091.

Mertikas, S., Tripolitsiotis, A., Donlon, C., et al., 2020. The ESA Permanent facility for altimetry calibration: monitoring performance of radar altimeters for Sentinel-3A, Sentinel-3B and Jason-3 using transponder and sea-surface calibrations with FRM standards. Remote Sensing 12 (16), 2642. https://doi.org/10.3390/rs12162642, URL: https://www.mdpi.com/2072-4292/12/16/2642. Number: 16 Publisher: Multidisciplinary Digital Publishing Institute.

Moreau, T., Cadier, E., Boy, F., et al., 2021. High-performance altimeter Doppler processing for measuring sea level height under varying sea state conditions. Adv. Space Res. 67 (6), 1870–1886. https://doi.org/10.1016/j.asr.2020.12.038, URL: https://www.sciencedirect.com/science/article/pii/S027311772030911X.

Moreau, T., Tran, N., Aublanc, J., et al., 2018. Impact of long ocean waves on wave height retrieval from SAR altimetry data. Adv. Space Res. 62 (6), 1434–1444. https://doi.org/10.1016/j.asr.2018.06.004, URL: https://linkinghub.elsevier.com/retrieve/pii/S0273117718304708.

Phalippou, L., Demeestere, F., 2011. Optimal retracking of sar altimeter echoes over open ocean: Theory versus results for siral2 data. In: 2011 Ocean Surface Topography Science Team (OSTST) meeting.

Phalippou, L., Enjolras, V., 2007. Re-tracking of SAR altimeter ocean power-waveforms and related accuracies of the retrieved sea surface height, significant wave height and wind speed. In: 2007 IEEE International Geoscience and Remote Sensing Symposium, pp. 3533–3536. https://doi.org/10.1109/IGARSS.2007.4423608. iSSN: 2153-7003.

Quartly, G.D., Srokosz, M.A., McMillan, A.C., 2001. Analyzing altimeter artifacts: statistical properties of ocean waveforms. J. Atmosph. Oceanic Technol. 18 (12), 2074–2091. https://doi.org/10.1175/1520-0426(2001)018<2074:AAASPO>2.0.CO;2, URL: https://journals.ametsoc.org/view/journals/atot/18/12/1520-0426_2001_018_2074_aaaspo_2_0_co_2.xml. Publisher: American Meteorological Society Section: Journal of Atmospheric and Oceanic Technology..

Raney, R., 1998. The delay/Doppler radar altimeter. IEEE Trans. Geosci. Remote Sens. 36 (5), 1578–1588. https://doi.org/10.1109/36.718861, Conference Name: IEEE Transactions on Geoscience and Remote Sensing.

Raney, R., 2012. CryoSat SAR-mode looks revisited. IEEE Geosci. Remote Sens. Lett. 9 (3), 393–397. https://doi.org/10.1109/LGRS.2011.2170052.

Ray, C., Martin-Puig, C., Clarizia, M., et al., 2015. SAR Altimeter Backscattered Waveform Model. IEEE Trans. Geosci. Remote Sens. 53, 911–919. https://doi.org/10.1109/TGRS.2014.2330423.

Rieu, P., Amraoui, S., Restano, M., 2021a. SMAP (Standalone Multimission Altimetry Processor). https://doi.org/10.5270/esa-cnes.sentinel-3.smap.

Rieu, P., Moreau, T., Cadier, E., et al., 2021b. Exploiting the Sentinel-3 tandem phase dataset and azimuth oversampling to better characterize the sensitivity of SAR altimeter sea surface height to long ocean waves. Adv. Space Res. 67 (1), 253–265. https://doi.org/10.1016/j.asr.2020.09.037, URL: https://linkinghub.elsevier.com/retrieve/pii/S0273117720306840.

Scagliola, M., Dinardo, S., Fornari, M., 2015a. An extended analysis of along-track antenna pattern compensation for SAR altimetry. In: 2015 IEEE International Geoscience and Remote Sensing Symposium (IGARSS), pp. 1238–1241. https://doi.org/10.1109/IGARSS.2015.7325997. iSSN: 2153-7003.

Scagliola, M., Fornari, M., Tagliani, N., 2015b. Pitch estimation for cryosat by analysis of stacks of single-look echoes. IEEE Geosci. Remote Sens. Lett. 12 (7), 1561–1565. https://doi.org/10.1109/LGRS.2015.2413135, Conference Name: IEEE Geoscience and Remote Sensing Letters.

Smith, W.H.F., Scharroo, R., 2015. Waveform aliasing in satellite radar altimetry. IEEE Trans. Geosci. Remote Sens. 53 (4), 1671–1682. https://doi.org/10.1109/TGRS.2014.2331193, Conference Name: IEEE Transactions on Geoscience and Remote Sensing.

Tran, N., Vandemark, D., Zaron, E.D., et al., 2021. Assessing the effects of sea-state related errors on the precision of high-rate Jason-3 altimeter sea level data. Adv. Space Res. 68 (2), 963–977. https://doi.org/10.1016/j.asr.2019.11.034, URL: https://www.sciencedirect.com/science/article/pii/S0273117719308427.

Vachon, P.W., Krogstad, H.E., Paterson, J.S., 1994. Airborne and spaceborne synthetic aperture radar observations of ocean waves. Atmos. Ocean 32 (1), 83–112. https://doi.org/10.1080/07055900.1994.9649491, URL: http://www.tandfonline.com/doi/abs/10.1080/07055900.1994.9649491.

Valenzuela, G.R., 1978. Theories for the interaction of electromagnetic and oceanic waves — A review. Bound.-Layer Meteorol. 13 (1), 61–85. https://doi.org/10.1007/BF00913863.

Wingham, D., Francis, C., Baker, S., et al., 2006. CryoSat: A mission to determine the fluctuations in Earth's land and marine ice fields. Adv. Space Res. 37 (4), 841–871. https://doi.org/10.1016/j.asr.2005.07.027, URL: https://linkinghub.elsevier.com/retrieve/pii/S0273117705009348.

Wingham, D., Phalippou, L., Mavrocordatos, C., et al., 2004. The mean echo and echo cross product from a beamforming interferometric altimeter and their application to elevation measurement. IEEE Trans. Geosci. Remote Sens. 42 (10), 2305–2323. https://doi.org/10.1109/TGRS.2004.834352, Conference Name: IEEE Transactions on Geoscience and Remote Sensing.

Zaron, E.D., deCarvalho, R., 2016. Identification and reduction of retracker-related noise in altimeter-derived sea surface height measurements. J. Atmosph. Oceanic Technol. 33 (1), 201–210. https://doi.org/10.1175/JTECH-D-15-0164.1, URL: https://journals-ametsoc-org.tudelft.idm.oclc.org/view/journals/atot/33/1/jtech-d-15-0164_1.xml. Publisher: American Meteorological Society Section: Journal of Atmospheric and Oceanic Technology.